

MYOCARDIAL BIOMECHANICAL EFFECTS OF FETAL AORTIC VALVULOPLASTY INTERVENTION

Laura Green¹, Wei Xuan Chan^{1,2}, Andreas Tulzer^{3,4}, Gerald Tulzer^{3,4}, Choon Hwai Yap¹

1 Department of Biomedical Engineering, Imperial College London, London, UK

2 BHF Centre of Research Excellence, Imperial College London, London, UK

3 Department of Pediatric Cardiology, Children's Heart Center Linz, Kepler University Hospital, Linz, Austria

4 Medical Faculty, Johannes Kepler University Linz, Altenberger Strasse 69, 4040 Linz, Austria

Corresponding Author:

Choon Hwai Yap,

L2 Bessemer Building, South Kensington Campus,

Imperial College London, London, SW7, 2AZ, UK

Email: c.yap@imperial.ac.uk

ABSTRACT

Fetal critical aortic stenosis with evolving hypoplastic left heart syndrome (CAS-eHLHS) can progress to a univentricular (UV) birth malformation. Catheter-based fetal aortic valvuloplasty (FAV) intervention can resolve the stenosis and reduce the likelihood of progression to malformation. However, we have limited understanding of the biomechanical impact of FAV intervention and of subsequent LV responses. To address this, we performed image-based finite element (FE) modelling of 4 CAS-eHLHS fetal hearts, by performing iterative simulations to match image-based characteristics, to then back-compute physiological parameters. We used pre-FAV simulations to conduct virtual intervention and compared pre-FAV to post-FAV simulations. Virtual intervention simulations showed that FAV generally enabled partial restoration of several physiological features towards healthy levels, including increased stroke volume and myocardial strains, reduced aortic valve (AV) and mitral valve regurgitation (MVR) velocities, reduced LV and LA pressures, and reduced peak myofiber stress. FAV intervention often leads to aortic valve regurgitation (AVr), our simulations showed that AVr could compromise the depressurization of LV and LA but could also significantly increase stroke volume and deformational stimuli to the myocardium. Investigation of post-FAV scans and simulations showed FAV intervention could only enable partial reduction of AV flow resistance. Further to this, the contractility of the LV and peripheral vascular resistance could change in response to intervention, preventing decreases in AV velocity and LV pressure, compared with what would be anticipated from stenosis relief. This suggested that case-specific post-FAV modelling is required to fully capture the functionality of the heart. Overall, image-based FE modelling could provide mechanistic details of the effects of FAV, but computational prediction of acute outcomes was difficult due to a patient dependent physiological response to FAV.

Keywords: *fetal aortic valvuloplasty, fetal aortic stenosis with evolving hypoplastic left heart syndrome, patient-specific finite element modelling, virtual intervention analysis.*

1.0 INTRODUCTION

Fetal hearts diagnosed with critical aortic stenosis with evolving hypoplastic left heart syndrome (CAS-eHLHS) present physiological, functional and morphological aberrations, such as elevated LV pressure, reduced LV stroke volume, retrograde transverse aortic arch flow, reduced myocardial strains, globular left ventricle (LV) structures, endocardial fibroelastosis and monophasic mitral valve (MV) inflow (Freud et al., 2014; Friedman et al., 2014; Ishii et al., 2014; Mäkitallio et al., 2006; Tulzer et al., 2022). Such aberrations can lead to adverse remodeling in gestation, with a natural history study showing there to be a 73% likelihood of progression from CAS-eHLHS to hypoplastic left heart syndrome (HLHS) by the time of birth (Gardiner et al., 2016; Mäkitallio et al., 2006).

Fetal aortic valvuloplasty (FAV) intervention, is a mid-gestation in-utero catheter-based intervention, undertaken on CAS-eHLHS patients to widen the stenotic aortic valve (AV). Under ultrasound guidance the balloon catheter is inflated across the stenotic AV multiple times, to widen the valve, allowing increased blood flow, with the intention to promote healthier development in gestation. Patient selection criteria for FAV intervention varies among institutes, however, commonly if the fetus meets the criteria for evolving hypoplastic left heart syndrome (eHLHS), which is moderate to severe LV dysfunction, retrograde aortic arch flow and the presence of left-to-right foramen ovale shunting (Friedman et al., 2018), with the inclusion of functional metrics such as an LV long axis Z score >-1.0 (Tulzer et al., 2022), the fetus will be selected for FAV intervention. Through retrospective studies FAV intervention has been shown to promote healthier development in gestation, by reducing the likelihood of a HLHS outcome (Friedman et al., 2018; Gardiner et al., 2016; Mäkitallio et al., 2006; Tulzer et al., 2022).

Following a technically successful FAV intervention, LV myocardial strains were shown to increase (Ishii et al., 2014) and LV function was shown to significantly improve (Wohlmuth et al., 2016). The functional improvements, post-FAV, highlight the LVs ability to biomechanically respond to the essentially mechanical intervention of FAV. However, there is still limited in-depth understanding of the biomechanical effects of FAV intervention on the LV myocardium. For example, it is not completely clear how much stenosis relief is generally achieved, how various extents of stenosis relief affect LV pressure, stroke volume and myocardial strains, and how much reduction of abnormally high LV and LA pressures can be achieved. Further, a side-effect of FAV intervention is aortic valve

regurgitation (AVr) (Arzt et al., 2011), as the valvuloplasty tend to damage the AV but the effects of AVr on myocardial biomechanics and function is unclear.

Image-based finite element (FE) computational modelling is a robust approach for simulating the contractile ability, pumping function, and biomechanics details of the heart (Shavik et al., 2018; Zheng et al., 2022, 2023), helping comprehend how the stresses, strains, stroke volume and pressure of the heart adapt due to disease remodeling or interventions. FE modelling of the fetal heart has previously aided better understanding of the biomechanics of the fetal heart as well (Green et al., 2022; Ong et al., 2020). Here, we performed image-based, patient-specific FE modelling of CAS-eHLHS fetal hearts to improve our understanding of the mechanistic effects of FAV on the fetal LV's function and biomechanics. We first performed virtual interventions based on pre-FAV scans to determine the effects of stenosis relief alone. We then compared the results from FE modelling of patient-specific pre- and post-FAV models to investigate specific physiological changes across FAV intervention.

2.0 METHODS

2.1 Image Acquisition

4D echocardiography images of 4 CAS-eHLHS fetal hearts pre- and post-FAV intervention were acquired using the GE Voluson E10 (GE Healthcare, Chicago, IL, USA) ultrasound machine. Images were taken in the spatio-temporal image correlation mode, at sweeps of 10-15s and a capture rate of 70-90 frames per second. All images were obtained with informed consent from the Kepler University Hospital, Austria, under Institutional Review Board protocol 1009/2017.

2.2 Patient Characteristics

The characteristics of the patients included in the study are described in Table 1. Virtual FAV intervention simulation methods used the age at FAV intervention, patient-specific post-FAV simulation methods used the age at the post-FAV scans.

Table 1. Patient characteristics of CAS-eHLHS cases before intervention. Y - yes, N - no, Dil – balloon dilation of the AV, RK - Ross-Kono procedure, NW - Norwood Procedure.

	Patient 1	Patient 2	Patient 3	Patient 4
Age at FAV (wks+days)	24+6	29+3	22+4	24+6
Age at Post-FAV Scan (wks+days)	25+0	30+2	22+6	25+0
Postnatal Circulation	BV	BV	UV	UV
Multiple FAVs	N	N	N	N
Bradycardia	Y	N	N	Y
Pericardial Effusion	N	N	N	N
LV Thrombus	N	N	Y	N
Hydrops	N	N	N	N
Postnatal Procedures	Dil.	RK	NW	NW

2.3 Image Processing

For patient-specific FE simulation of both pre-FAV and post-FAV LVs, 3D reconstructions of the LV myocardium, left atrium (LA) cavity and right ventricle (RV) cavity were first performed as previously reported (Green et al., 2022). Briefly, 2D slices were extracted from the 4D volume files, then binary segmentation of the myocardium was performed using a lazy snap algorithm (Li et al., 2004). 3D reconstruction was then performed with VMTK (www.vmtk.org), with the reconstructed geometries smoothed in Geomagic (Geomagic Inc., Morrisville, NC, USA). 3D motions of the LV, LA and RV were extracted using a validated cardiac motion estimation algorithm (Wiputra et al., 2020). Briefly, the algorithm models motion in the image with spatial b-spline of temporal Fourier, curve-fitted to the displacement fields from pair-wise image registration 3D images of consecutive time points. The final reconstructed LV geometries are depicted in Figure 1, where satisfactory tracking can be demonstrated by Supplementary Figure S1.

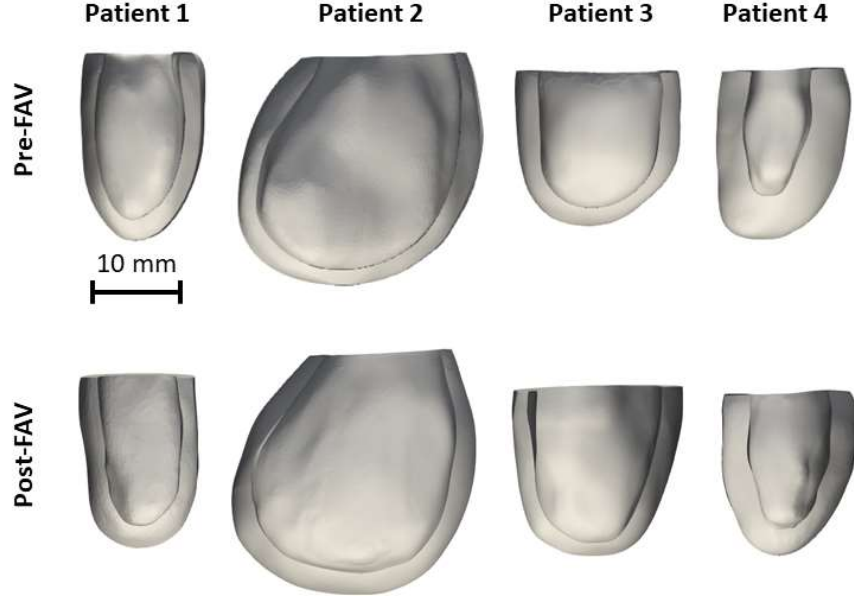


Figure 1. Patient-specific geometries, reconstructed from pre- and post-FAV echocardiographic data.

From the image-based cardiac motion estimation methods, myocardial strains could be computed using previous methods (Ren et al., 2023). LV myocardial engineering strains (Equation 1) were computed in both the longitudinal and circumferential directions along a mid-wall line, identified by averaging the epicardial and endocardial boundaries, from the 4-chamber or transverse echo view, using previously documented techniques. The mid-wall line was discretized into 100 elements, its motion was tracked, and changes in lengths of elements from end diastole to end systole were computed and spatially averaged,

$$\text{Engineering Strain} = \frac{\text{Length}_{\text{systole}} - \text{Length}_{\text{diastole}}}{\text{Length}_{\text{diastole}}}. \quad \text{Equation 1}$$

2.4 FE and Lumped Parameter Modeling Formulation

Image-based, patient-specific FE Modelling of fetal LV myocardial biomechanics was performed in accordance with our previous methodologies (Green et al., 2022; Ong et al., 2020), where the FE model is connected to a lumped parameter model to enable ventricular-vascular coupling (Pennati et al., 1997; Pennati. & Fumero., 2000).

The lumped parameter model used is based on Pennati et al.'s work (Pennati et al., 1997; Pennati. & Fumero., 2000), which underwent minor recalibration to more recent measurements of human fetal intracardiac

pressure (Johnson et al., 2000), and descending aorta pulse pressure (Versmold et al., 1981), as explained in our previous modelling study (Wong et al., 2022), where all model parameters are given. The lumped parameter model is scalable to a range of gestational ages, through a series of allometric equations.

The behaviour of the myocardium was described via a transversely isotropic Fung type passive stiffness model and an active tension model. The Fung type transversely isotropic passive stiffness model (Guccione et al., 1991) is described via the following strain energy function (W):

$$W = \frac{1}{2} C \left(e^{b_{ff} E_{ff}^2 + b_{xx} (E_{ss}^2 + E_{nn}^2 + E_{sn}^2 + E_{ns}^2) + b_{fx} (E_{fn}^2 + E_{nf}^2 + E_{fs}^2 + E_{sf}^2)} - 1 \right), \quad \text{Equation 2}$$

where C is the passive stiffness coefficient, E is the Green-Lagrange Strain, with subscripts f , s and n denoting the fiber, sheet and sheet-normal directions, respectively, and b is the stiffness exponent in specific directions specified by its subscript. The values assigned to stiffness parameters are shown in Table 2 and were obtained from a previous fetal heart FE study (Ong et al., 2020). Although myocardial stiffness could typically be scaled up or down via the stiffness coefficient (C in Equation 2) to model person-to-person variability in myocardial stiffness, Ong et al. showed that large changes to C had minimal effect on cardiac functionality and biomechanics (Ong et al., 2020). As such, we used the same stiffness model in Table 2 for all simulation scenarios in this study.

Guccione's active tension model, (P_{act}) (Guccione et al., 1993), is expressed as:

$$P_{act} = T_{0,LV} \frac{Ca_0^2}{Ca_0^2 + ECa_{50}^2} C_t, \quad \text{Equation 3}$$

where $T_{0,LV}$ describes the maximum fiber tension, which describes myocardial contractility and is back computed in the patient-specific optimisation methods. Maximum intracellular calcium concentration (Ca_0), described in Table 2, is the value of sarcomere length dependent calcium sensitivity (ECa_{50}) and is calculated as follows:

$$ECa_{50} = \frac{Ca_0}{\sqrt{\exp[B(l - l_0)] - 1}}, \quad \text{Equation 4}$$

where B describes the shape of peak isometric tension-sarcomere length relation, l is sarcomere length and l_0 , is the sarcomere length at no tension generation, all of which are documented in Table 2. C_t in Equation 3 is the temporal variation of the calcium activation model, described as:

$$C_t = \frac{1}{2}(1 - \cos \omega), \quad \text{Equation 5}$$

where ω was dependent on the cycle time, with the variation:

$$\omega = \begin{cases} \pi \frac{t}{t_0} & \text{when } 0 \leq t < t_0, \\ \pi \frac{t - t_0 + t_r}{t_r} & \text{when } t_0 \leq t < t_0 + t_r, \\ 0 & \text{when } t_0 + t_r \leq t, \end{cases} \quad \text{Equation 6}$$

where t_0 was the time to peak tension, calculated using the model specific cardiac cycle length and Mulieri et al.'s measured relationship between cardiac cycle and time to peak tension (Mulieri et al., 1992). t_r , was the relaxation time and was calculated using the following equation:

$$t_r = ml + b, \quad \text{Equation 7}$$

where m is the gradient of linear relaxation duration and b is the time intercept of linear relaxation duration, dependent on the degree of myocyte stretch, with parameter values also documented in Table 2.

Table 2. Finite element modelling parameters required for both the passive and active description of the myocardium.

Parameter	Symbol	Unit	Value
Passive stiffness coefficient	C	Pa	200
Stiffness coefficient in fiber direction	b_{ff}	-	29.9
Stiffness coefficient in sheet and sheet normal direction	b_{xx}	-	13.3
Stiffness coefficient in shear directions	b_{fx}	-	26.6
Shape of peak isometric tension-sarcomere length relation	B	μm^{-1}	4.75
Sarcomere length under no active tension	l_0	μm	1.58
Relaxed sarcomere length	l_r	μm	1.85
Time intercept of linear relaxation duration with sarcomere length	B	ms	-800
Gradient of linear relaxation duration with sarcomere length relaxation	m	$\text{ms} \cdot \mu\text{m}^{-1}$	524
Maximum intracellular calcium concentration	Ca_0	μM	4.35

The myocardium helix angle configuration was assumed to be the same for all patients and was assigned based on the average of 3 previous publications, which quantified the fetal helix angle configuration (Garcia-Canadilla et al., 2018; Nishitani et al., 2020; Ohayon et al., 1999). Therefore, the myocardium helix angle configuration was assumed to vary linearly from -52° at the epicardium to $+71^\circ$ at the endocardium.

To calculate the unloaded (zero chamber pressure) state of the LV, we adopted Finsberg et al.'s backward displacement method (Finsberg et al., 2018). This involves iteratively simulating the unloading of an initial diastolic LV geometry to the load-free state (estimated as the inverse deformation of loading of a similar pressure) followed by the diastolic pressure loading of the load-free state to end-diastolic state. During the iterative simulations, the pressure of the initial LV geometry is adjusted, and iterations were repeated until the end-diastolic state achieved the targeted pressure and volume. In CAS-eHLHS cases, the left atrium is often pressurized and enlarged (Tulzer et al., 2022). We performed patient-specific estimation of end-diastolic LA pressure, by assuming a linear relationship between LA size and pressure (LA compliance) (Wong et al., 2022).

LV myocardium models, displayed in Figure 1, were meshed with a minimum of 2,500 quadratic tetrahedral elements, which was sufficient for mesh convergence as shown in our previous study (Ong et al., 2020). The formal FE simulation was performed by minimizing the weak formulation of a Lagrangian functions described by Shavik et al., which enforces tissue stress equilibrium, incompressibility, and a specific cavity volume to yield cavity pressure, using the Newton Solver in the FEniCS software (Shavik et al., 2018). The boundary conditions were like that previously reported (Shavik et al., 2018), with the basal plane of the LV constrained in the longitudinal direction and a weak 90 Pa spring applied to the entire epicardium at the load-free state, to constrain translational motion of the model and to imitate the behaviour of the surrounding tissues. The model was executed for 30 cycles, to ensure steady state was achieved.

2.5 Virtual FAV Intervention Methods

Virtual FAV was performed by modulating the lumped parameter model of the patient-specific image-based FE models of pre-FAV fetal LVs. To conduct patient-specific FE modelling of pre-FAV LVs, the lumped parameter model was first scaled to the specific pre-FAV gestational age, and then iterative FE simulations was conducted while varying AV, MV inflow and MVr flow resistances and peak myocardial active tension, until the simulated valvular pressure gradients (ΔP) matched echo-measured gradients calculated using the simplified Bernoulli equation and doppler velocities, and the simulated stroke volume matched that from echo images. Through this matching process, the patient-specificity of the model was maintained, and the valve resistances and peak myocardial active tension could be back-computed. In this process, valve resistances were modelled as,

$$\Delta P = R \cdot Q + K \cdot Q^2 + L \cdot \frac{\delta Q}{\delta t}, \quad \text{Equation 8}$$

where ΔP is the pressure difference across the valve, Q is the volume flow rate, R is the resistance coefficient, K is the valvular dissipative coefficient, and L is the valvular inertial coefficient. During the optimization and adjustment of valve resistances, only K was adjusted while R and L were kept constant as a simplification, to avoid convergence issues and non-unique solutions. Peak myocardial active tension was initially set as 60 kPa based on the upper limit of experimental measurements (Racca et al., 2016). If less than 10% error between patient data and simulation results could not be achieved, the age scaling of the lumped parameter model was adjusted, and the iterative matching process repeated. This age scaling adjustment represented a way to adjust for fetal body size variability or body developmental maturity.

From the optimised pre-FAV models, AV resistance was reduced to simulate the widening the AV and relief of stenosis via FAV intervention, by reducing valvular coefficient, K . A few magnitudes of reduction were simulated, between the resistance value of pre-FAV LV to that of an age-matched healthy LV, as defined in our lumped parameter model (Wong et al., 2022). The process of simulating relief of the AV was then repeated for two levels of AVr severity. This was because a range of AVr velocities was possible, as indicated by the relatively wide standard deviation of regurgitation velocity (1.92 ± 0.87 m/s) from our clinical database of 44 cases (Supplementary Material Figure S2). Two levels of AVr severity were investigated: moderate AVr, where regurgitant valve flow resistance was equal to the AV antegrade flow resistance, and high AVr, where regurgitant valve resistance was 10x that of the AV antegrade resistance.

A sensitivity analysis was performed to assess how other physiological features (such as a change in heart rate, increased vascular resistance, and increased myocardial contractility) affected valve velocities and stroke volume, and how they contributed to the match between virtual intervention and image-based measurements.

2.6 Patient-Specific Post-FAV Intervention Methods

The patient-specific post-FAV FE modelling was conducted under the same protocol as that for pre-FAV FE modelling, with the addition of matching the patient-specific AVr ΔP , as post-FAV hearts have AVr but pre-FAV hearts do not.

2.6 Computational Biomechanics Characteristics

From the FE and lumped parameter modelling methods a series of biomechanics parameters can be output to aid analysis of the models generated. Stroke volume was extracted based on the cardiac motion estimation algorithm, peak LV and LA pressure were extracted directly from the computational methods. Peak myofiber stress was calculated by computing the stress in the myofiber direction (direction of the helix angle), and then performing spatial averaging over the entire myocardial volume, as follows,

$$\text{Peak Myofiber Stress} = \frac{1}{V} \int_V \vec{f}_d \sigma \vec{f}_d dV, \quad \text{Equation 9}$$

where V is the volume of the myocardium, \vec{f}_d is the unit vector in the myocardial direction, and σ is the stress tensor at peak systole. Work done, was quantified by calculating the area inside the PV loop and describes the ability of the LV to eject fluid.

3.0 RESULTS

3.1 Effects of FAV Intervention on Fetal Heart Biomechanics and Function

The pre-FAV simulations were iteratively conducted to optimize for patient-specific characteristics, such that myocardial contractility and LV heart valve resistances were adjusted to ensure a good fit with imaged stroke volume and Doppler valve gradients for AV and MV antegrade and regurgitation flows respectively. In essence, this was a back computation of the myocardial contractile force generation and AV stenosis severity. Supplementary Table S1 showed that a good match was obtained.

From the optimized image-based FE simulations for pre-FAV scenario, virtual intervention was simulated by reducing flow resistance of the stenotic AV, and by introducing AVr, which commonly occurred after the intervention (Bradford et al., 2022). The virtual intervention altered only AV flow resistances, every other parameter was kept at the pre-FAV level, so that we could isolate and understand the biomechanical effects specific to this modulation of the AV. In our previous study, we found that the reduction in stenosis via FAV intervention can be variable and span a range of magnitudes (Wong et al., 2023). As such, we conducted simulations over a range of reduced AV flow resistances.

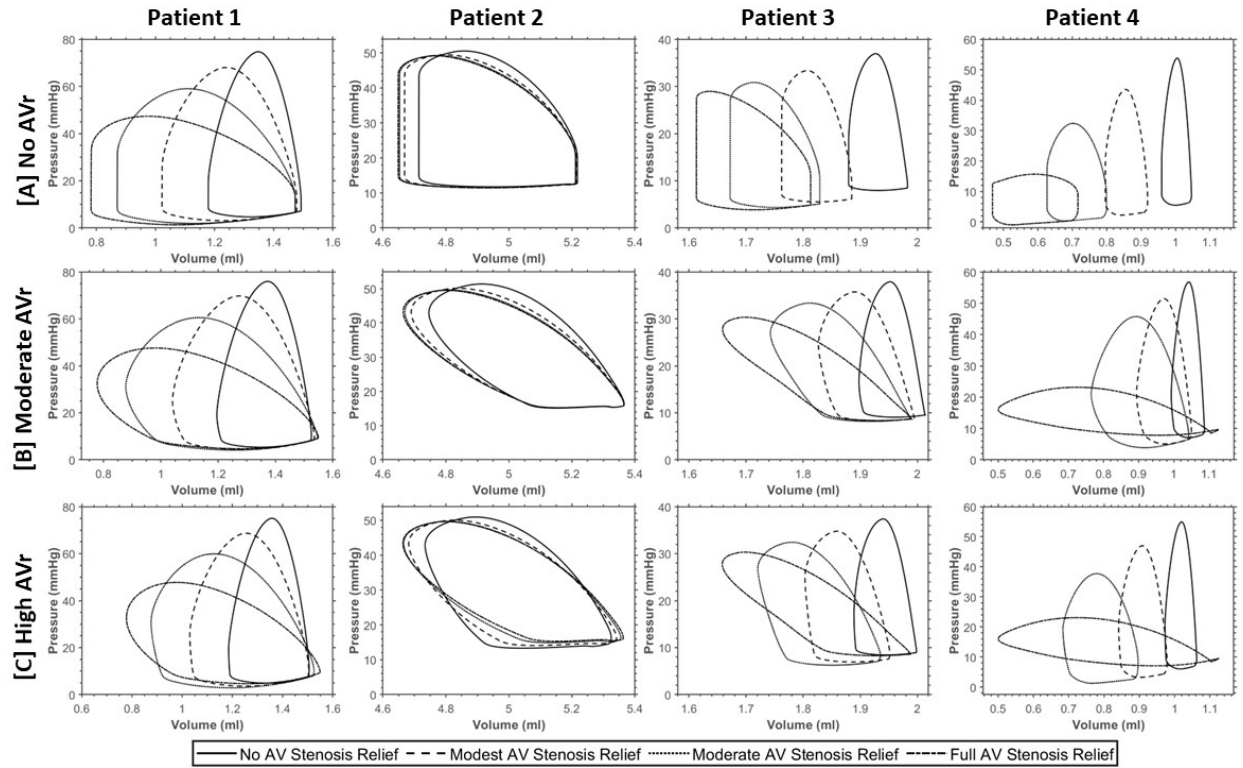


Figure 2. PV loops from patient-specific pre-FAV scans of 4 patients, along with those from simulations of virtual FAV intervention. [A], [B], and [C] rows corresponded to simulations assuming no AVr after FAV intervention, moderate AVr after FAV intervention, and high AVr after FAV intervention, respectively. Simulations assumed 3 levels of stenosis relief resulting from FAV which were modest, moderate, and full relief of stenosis.

PV loop results from virtual FAV simulations are shown in Figure 2. Generally, we observed that relieving the AV stenosis led to reduced LV pressure and greater stroke volume, the extent of which directly depended on the level of stenosis relief. Different patients also experienced different extents of LV depressurization and stroke volume augmentation, which were likely dependent on the stenosis severity. Patient 2, for example, had a milder stenosis, judging from the lower back-computed valve resistance (Table 3), and thus did not undergo a drastic change after FAV. When AVr was introduced (Figure 2B and C), the LV effectively had regurgitation in both the mitral and aortic valves, and the PV loops no longer exhibited isovolumic periods and appeared slanted. AVr caused the LV to fill more during diastole, leading to an increase in end-diastolic volume, thus increasing stroke volume. This increase could be drastic, like that observed in Patients 3 and 4. AVr also increased end-diastolic pressure, due to the greater filling volume, and slightly increased peak systolic pressure, likely due to additional engagement of contractile

myofibers, resulting from the greater filling volume. This meant that the atria pressure could fail to decrease from the diseased baseline, and in some instances increase further.

Figure 3 shows further virtual FAV results for the same patients. Here, the parameter values for the healthy fetal heart are indicated by the horizontal grey dotted line. These age dependent healthy parameters were obtained from Parasuraman et al. for AV velocity (Parasuraman et al., 2013), from Johnson et al. for intracardiac pressure measurements during peak systole and end diastole (Johnson et al., 2000), where the diastolic LV pressures were assumed to indicate peak LA pressures, and from Devore et al. for stroke volume measurements (Devore et al., 2019). Healthy fetal heart myofiber stresses have not been reported in literature. We therefore estimated healthy fetal LV myofiber stress via image-based simulations of 6 healthy fetal hearts, as explained in Supplementary Section 3.0, where we found that myofiber stresses were 12.19 ± 2.62 kPa and appeared to be invariant with age (Supplementary Figure S3).

Generally, the reduction in AV resistance (from the right of each plot to the left) produced substantial reductions in AV velocity (Figure 3A-D) and LV pressure (Figure 3M-P), due to the relief of the stenotic flow and LV fluid congestion, but the extent of the reduction was dependent on how high the pre-FAV AV velocity was. For example, for Patient 2, the initial AV velocity and LV pressure were only modestly high, and thus the reduction was not as drastic. FAV also generally decreased MVr velocity (Figure 3E-H), due to more AV outflow after FAV intervention, but the effects on MVr were modest compared to those on AV velocity and LV pressure. Along with the improved AV outflow, stroke volumes substantially improved (Figure 3I-L), and along with the reduction in LV pressure, myofiber stresses were substantially reduced (Figure 3U-X). Again, the changes with FAV depended on the initial disease severity. Thus, overall, substantial restoration of LV biomechanics and function towards the healthy state could be achieved with FAV intervention, if stenosis relief was robust, pointing to the robust benefits that could be brought by FAV intervention.

The effects of FAV intervention on LA pressure were more complex (Figure 3Q-T) and depended on the severity of AVr after FAV. If there was no AVr, decreased AV resistance generally led to depressurization of the LA. However, with AVr, the LA pressure did not depressurize effectively. This was because when AVr was present in the virtual FAV simulations, end diastolic pressure of the LV was higher, which was then passed back to the LA through

the open MV. Here, we assumed that AVr severity was dependent on the extent of stenosis relief (AVr valve dissipative coefficient was a fixed fraction of that of AV forward flow), which is a likely scenario as a more robust valvuloplasty tends to induce more valve damage. For this reason, the effect of AVr preventing LA depressurization was more obvious at lower AV resistances in Figure 3Q-T (towards the left side of the plots, where there was more stenosis relief). For scenarios with strong MVr and high MVr velocities, this above effect of AVr on LA pressure was weak (Patient 1 and 2), and the difference between AVr scenarios were not too far from the no AVr scenario. This was because strong MVr flow caused LA pressure buildup even without AVr. Conversely, for patients with lower MVr velocities (Patients 3 and 4), the presence of AV regurgitation made substantial difference for LA pressure. Thus, it was likely that in many cases, the acute effect of FAV would not include a depressurization of the LA. However, if the AVr improved/resolved over subsequent gestational development, which has been observed in literature (Marshall et al., 2005), LA pressure would likely depressurize.

The presence of AVr also had significant effects on LV pressure and stroke volume. Regurgitation could further elevate stroke volume beyond the elevation brought by stenosis relief (Figure 3I-L). Complete relief of stenosis without AVr could bring stroke volume up by 12-190%, while complete relief of stenosis with high AVr increases stroke volume by 20-633%. While the improvements to stroke volume did not correspond directly to the same improvement in aortic output, as much of the stroke volume is MVr into the LA, it nonetheless improved the motion of the LV and increased deformational stimuli. Given that stroke volumes of CAS-eHLHS can be very low pre-FAV, as shown in Figure 3I-L, this additional motion and deformational stimuli provided could be useful to encourage growth response of the LV to avoid a UV birth outcome. As for LV pressure, the effect of AVr on elevating LV pressure was greater if the baseline LV pressure was low, like that observed in Patients 3 and 4, and was milder if the baseline LV pressure was high, like that observed in Patients 1 and 2.

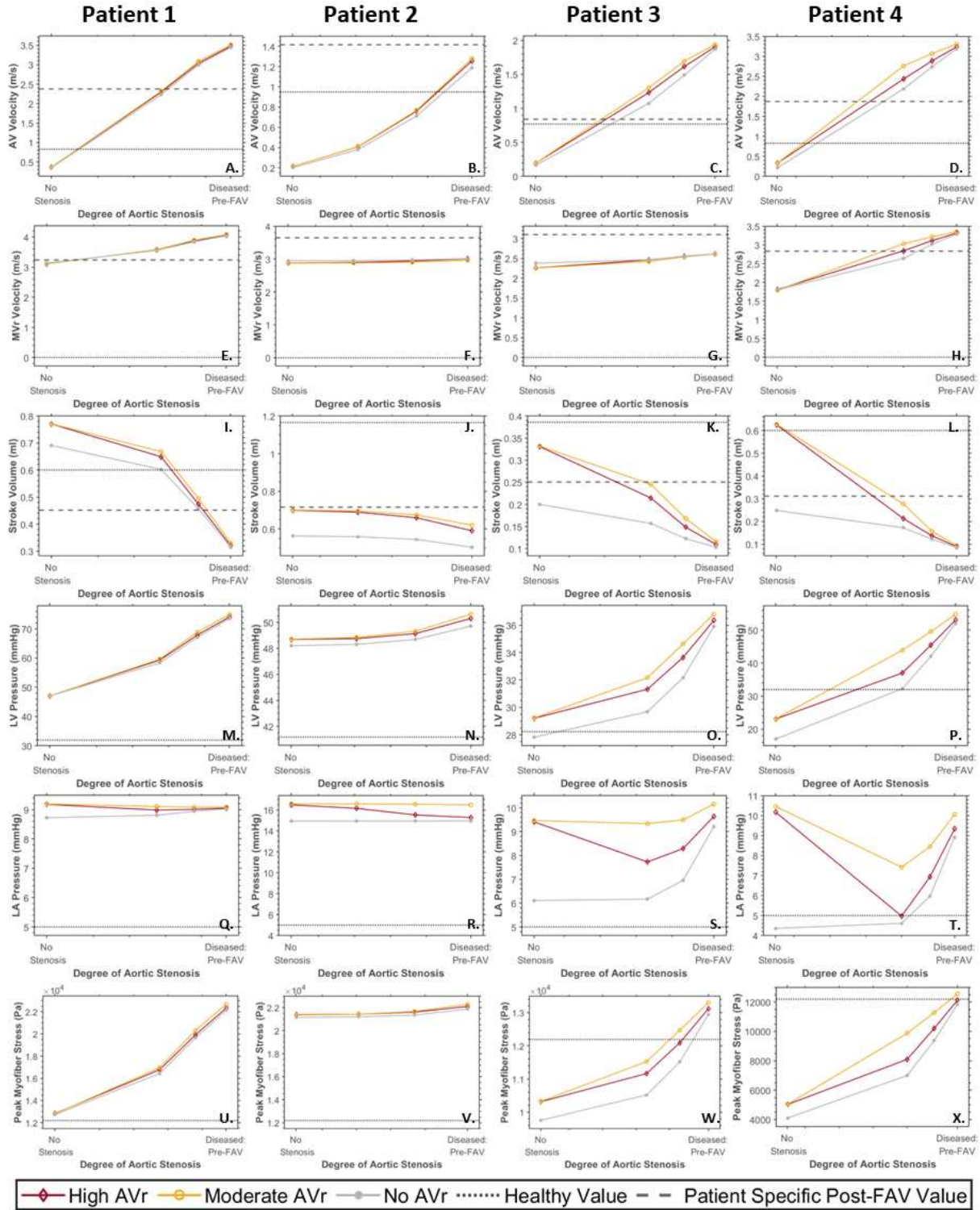


Figure 3. Cardiac physiological characteristics after virtual interventions, from image-based FE simulations, including (A-D) AV velocity, (E-H) MV regurgitation (MVr) velocity, (I-L) stroke volume, (M-P) Peak systolic LV Pressure, (Q-T) end diastolic LA pressure, (U-X) Peak Myofiber stresses. Characteristics were plotted across a range

of aortic stenosis resistances, with the right end of the horizontal axis being the baseline diseased condition, while the left end of the axis being the no stenosis scenario, where AV resistance was that of an age-matched healthy subject. 3 levels of AV regurgitation (AVr) were simulated: no stenosis (gray line), moderate AVr (yellow line), and high AVr (red line). Values for an age-matched healthy subject were plotted in dotted line, while that derived from image-based FE simulations of post-FAV scans for the same subjects were plotted in dashed line.

3.2 Sensitivity Analysis of Virtual FAV Intervention

In Figure 3, the grey dashed lines present in Figures 3A-L marked the echocardiographic measurements from follow up scans of the same patients very shortly after FAV intervention. Results from the virtual intervention simulations (in red, yellow or gray), however, did not always intersect with this post-FAV measurement (dashed lines). For 4 plots, such as for AV forward flow velocity for Patient 2 (Figure 3B), and MVr velocity for Patients 2 and 3 (Figure 3F and G), an intersection was not found, suggesting that the range of post-FAV scenarios simulated did not match the actual post-FAV situation. Since the virtual intervention emulated only changes to the AV flow resistances, without a change to other physiology, such as contractility and peripheral vascular resistances, the mismatch in some cases suggested that there were other physiological changes in addition to the changes to AV resistances. For example, it was likely that Patient 2s myocardial contractility increased post-FAV, such that the post-interventional AV velocity was higher than those predicted by virtual FAV simulations.

We thus performed sensitivity analysis, to understand how certain physiological changes after FAV intervention will impact the fetal heart, to better understand what were the physiological factors that could account for the mismatch. We conducted this for Patient 2, as this was the patient with the worst match between virtual FAV simulations and actual post-FAV measurements. Here, we used the virtual FAV simulation that had a moderate reduction in AV stenosis and high AVr, as the baseline simulated case, and explored how an altered heart rate, increased peripheral vascular resistance, and contractility affected cardiac behavior.

Figure 4 showed the results of the sensitivity analysis. Results showed that two standard deviations or 16.46% increase in heart rate (BPM) during the virtual FAV simulation yielded little change to AV and MVr velocities but caused mild decreases in AVr velocity and stroke volume. Further, a 100% increase in systemic vascular resistance caused a decrease in AV and AVr velocity and stroke volume but did not affect MVr velocity. Finally, a 50%

increase in myocardial contractile force generation caused substantial increases in AV, AVr, and MVr velocities, and stroke volume.

Due to the small magnitudes of effects, heart rate is unlikely to explain the mismatch between FAV simulation and post-FAV measurements. Further, our data of a cohort of 44 FAV cases demonstrated that there was no significant change to the heart rate from pre- to post-FAV ($1.77 \pm 8.23\%$ change from 0.65 ± 5.82 bpm at pre-FAV), as shown in Supplementary Figure S2. In fact, for Patient 2, the heart rate did not change from pre- to post-FAV, measuring at 133 BPM during both scans. Contractility, however, had large effects, and increased all 4 measurements in Figure 4 closer to the actual post-FAV measurements. An increase in contractility was thus likely to have occurred after FAV intervention, which could explain the mismatch. However, increasing contractility to improve the virtual FAV intervention comparison with imaged AV, AVr and MVr velocities, would elevate stroke volume beyond the actual post-FAV measurements, it was thus likely that an increase in peripheral resistance accompanied the increase in contractility to bring stroke volume down. Since FAV intervention increased general cardiac output of the heart (Supplementary Material Table S3), it seemed reasonable to expect peripheral vessels to respond to the higher flow with a stronger vascular tone and pose higher resistance to flow.

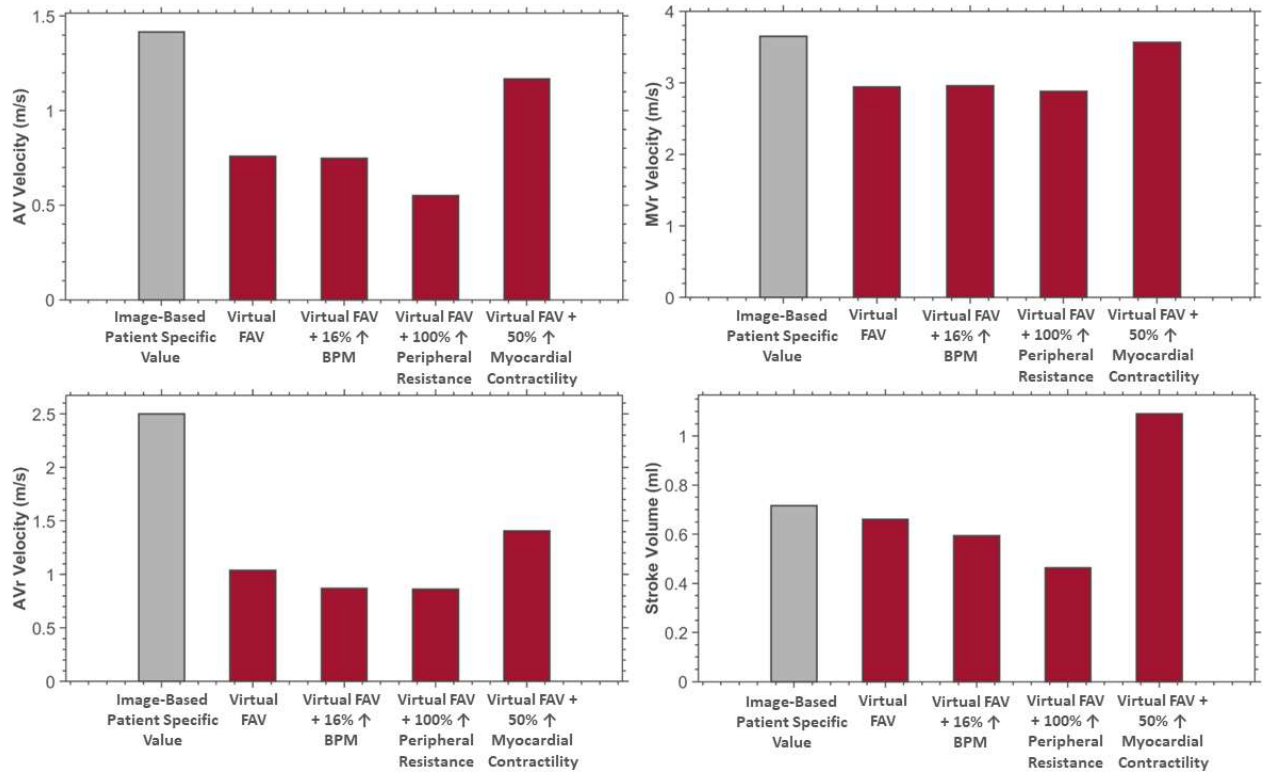


Figure 4. Sensitivity analysis on how change physiological changes to heart rate, peripheral vascular resistance and heart rate affected valve velocities and stroke volume of the post FAV fetal heart for Patient 2. Red bars correspond to virtual FAV simulations assuming high AVr and moderate stenosis reduction by FAV, with and without such physiological changes. The grey bar plots the actual post-FAV echo measurement value for Patient 2.

3.3 Patient-Specific Post-FAV Intervention Biomechanics

To better understand the patient-specific actual post-FAV biomechanics, we conducted image-based simulations on the same patients from post-FAV scans. Figure 5 showed the post-FAV PV loops compared to pre-FAV loops, demonstrating that generally, FAV substantially increased stroke volume. However, interestingly, peak systolic pressure did not always reduce from its high diseased magnitude, despite the reduction in AV stenosis. While pressure was reduced in Patients 1 and 4, it was elevated in Patients 2 and 3. This was likely due to changes to myocardial contractility. While stenosis relief reduced pressure, increased contractile forces elevated it, and the net effect could be an increase for some cases. For all cases, the post-FAV peak systolic LV pressure remained elevated and did not come down to the healthy LV level, depicted by the horizontal dotted line in Figure 5.

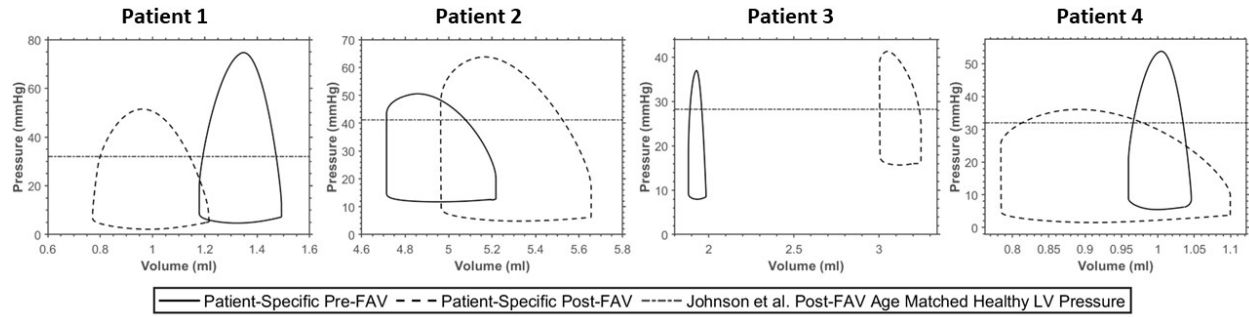


Figure 5. Pre-FAV and post-FAV PV loops, extracted from patient-specific modelling methods, compared to published peak systolic LV pressure measurements of age-matched (to post-FAV age) healthy fetal hearts (Johnson et al., 2000).

Table 3 shows the back-computed valve dissipative coefficients for antegrade AV and MV flow, which reflected flow resistances, for the pre- and post-FAV models. These results demonstrated that FAV typically created substantial relief in AV stenosis and substantially reduced AV resistance, but flow resistances remained substantially higher than those of the age-matched healthy fetal hearts. Patient 2 was an exception, where the initial AV resistance was not exceptionally high, and FAV intervention only decreased the AV resistance slightly. The range of AV resistances considered by our virtual FAV simulations are also given in Table 3, and it could be observed that they encompassed the actual post-FAV resistance, demonstrating that our virtual intervention covered the appropriate stenosis relief scenarios.

The post-FAV functional and biomechanics characteristics compared to their corresponding pre-FAV values are shown in Figure 6, the values of which are given in Supplementary Table S3. As with Figure 5, we could observe here that FAV resulted in an increase in stroke volume (Figure 6A). Consequent to larger stroke volume, longitudinal strain (Figure 6I), and circumferential strain (Figure 6J) increased as well for all patients, which demonstrated the ability of FAV intervention to enable greater myocardial deformations, which could be important for healthier subsequent cardiac development. For the remaining characteristics investigated, including EDV, AV velocity, MVr velocity, LV pressure, peak myofiber stress, myocardial contractility and work done (Figure 6B-H), pre- to post-FAV trends were not uniform across patients.

As discussed above, LV pressure (Figure 6E) did not always reduce, and likely depended on contractility and the extent of AV stenosis relief. For example, a substantial post-FAV increase in myocardial contractile forces was found for Patient 2 (Figure 6G), and a consequent post-FAV elevation in LV pressure was observed. However, this elevation in LV pressure in Patients 2 and 3 was likely responsible for the post-FAV elevation in their myocardial stresses, and in MVr velocities, as higher LV pressure induced higher wall stresses and drove stronger MVr. In the same way, despite the reduction in AV flow resistance, AV velocity did not always reduce, and was elevated post-FAV for Patient 2. Again, this could be attributed to its post-FAV elevation in contractility. While FAV intervention led to a reduction in AV stenosis brought about by a reduced AV velocity towards lower healthy values, elevated contractility and increased LV outflow could then increase AV velocities, and the net effect could be an increase in AV velocity, like that observed in Patient 2. As for the pre- to post-FAV trends observed for EDV, they are likely related to LV pressure, as increases in LV pressures, could lead to LV distention and influence the severity of AV and MVr, which would then determine the extent of diastolic filling.

Among the 4 cases, there was substantial variability, with varying extent of changes to myocardial contractility, LV pressure, AV velocities and other characteristics. The individuality of each patients' results highlighted the complex nature of CAS-eHLHS biomechanics and the impact FAV intervention can therefore have.

Table 3. Valve dissipative coefficient (indicating flow resistances) in patient-specific, image-based pre- and post-FAV simulations that enabled the best match between imaged and simulated stroke volumes and valve velocities. Valve coefficient from an age-matched healthy fetal heart, determined via our scalable fetal circulatory lumped parameter model for healthy fetuses (Wong et al., 2022), were included for comparison, as well as valve coefficients used in our virtual intervention simulations, which ranged from the best fit pre-FAV diseased value to that of healthy LV value.

ID	Scenario	AV Valvular Dissipative Coefficient (mmHg ms ² /ml)	MV Valvular Dissipative Coefficient (mmHg ms ² /ml)
Patient 1	Pre-FAV	13.69	0.1168
	Post-FAV	3.513	0.1210
	Age-matched Healthy LV	0.006174	0.01235
	Virtual Intervention	0.006174 to 13.69	0.1168
Patient 2	Pre-FAV	0.2135	0.02420
	Post-FAV	0.2052	0.03817

	Age-matched Healthy LV Virtual Intervention	0.002705 0.002705 to 0.2135	0.005411 0.02420
Patient 3	Pre-FAV	33.07	0.2960
	Post-FAV	0.2618	0.1247
	Age-matched Healthy LV Virtual Intervention	0.01008 0.01008 to 33.07	0.02015 0.2960
Patient 4	Pre-FAV	151.2	2.9235
	Post-FAV	1.6222	0.2030
	Age-matched Healthy LV Virtual Intervention	0.006174 0.006174 to 151.2	0.01235 2.9235

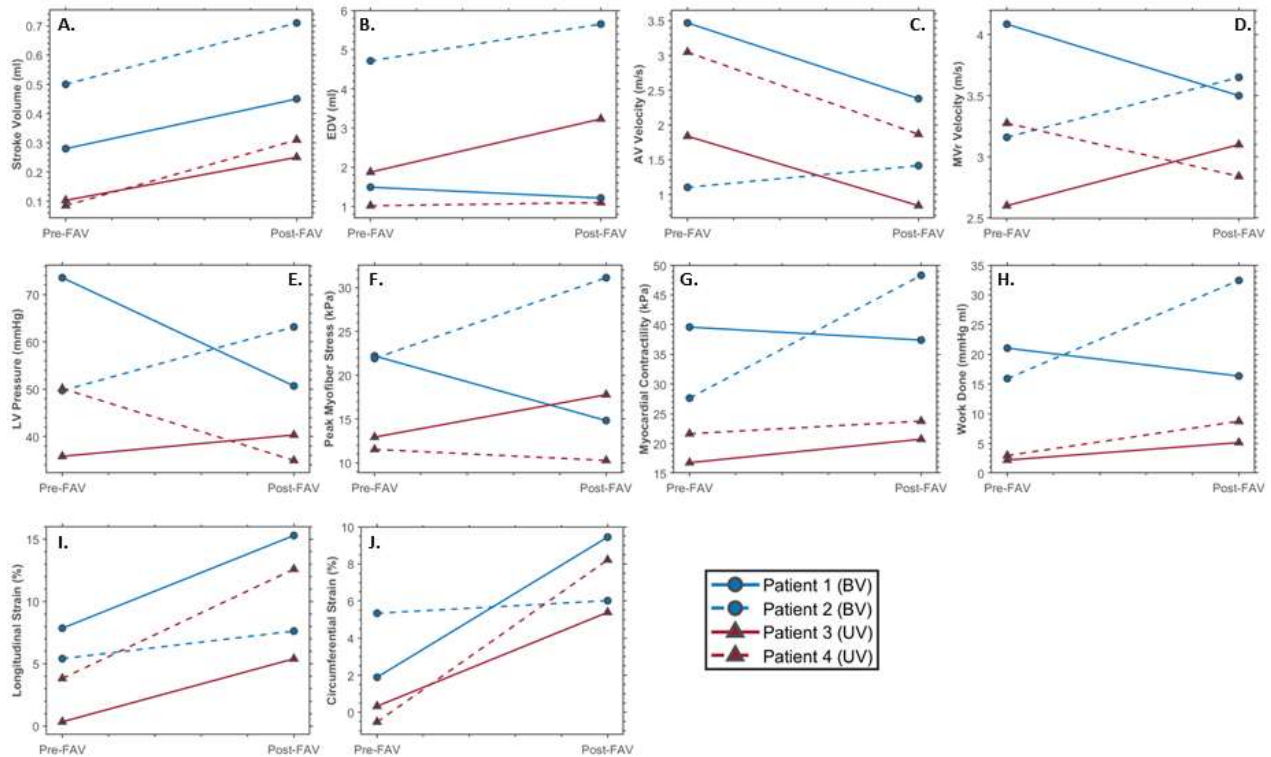


Figure 6. Pre-FAV versus post-FAV fetal LV characteristics. Stroke volume, EDV, valve velocities, and strains were measured via echo, while LV pressure, myofiber stress and contractility, and work done by the LV were back-computed via our iterative patient-specific FE computational modelling.

4.0 DISCUSSION

In this study we performed virtual FAV intervention, to comprehend the effect of FAV intervention on the biomechanics and function of the fetal LV. We studied this with two approaches. First, we performed simulations based on pre-FAV echo images, and then performed virtual FAV intervention by imposing a reduction in AV flow and introducing AVr. This was an idealized approach, assuming that only the AV is affected by FAV intervention and that

there are no other physiological responses, which served the purpose of elucidating the mechanistic effects of AV stenosis relief alone. Secondly, we performed simulations based on post-FAV images, to compare them to pre-FAV simulations, to understand the overall changes.

Diseased CAS-eHLHS LVs typically had high pressures and tissue stresses, and very low myocardial strains and stroke volume. They further had high atrial pressure and an enlarged LA (Pickard et al., 2020; Tulzer et al., 2022). This unusual biomechanical environment likely prevented normal development of the LV and LA. Our virtual FAV simulations showed that by relieving AV stenosis, FAV could depressurize the LV, reduce abnormally high AV velocities, reduce MVr severity, increase stroke volume, reduce myocardium tissue stresses, and, if AVr was not present, reduce LA pressure as well. All these represented partial normalizations of cardiac function and biomechanics, enabling lower stresses and increased deformational stimuli of myocardial tissue, and were thus likely beneficial for the subsequent development of the heart, to avoid progression to a univentricular birth outcome.

However, a complexity in this investigation was the presence of AVr, which was very common after FAV (Bradford et al., 2022). Virtual intervention simulations showed that the presence of AVr could dampen the ability of the LV and LA to depressurize, and depending on regurgitation severity, could even increase LA pressure. This was because AVr brought the higher aortic pressure into the LV, through regurgitation during diastole, and the higher pressure was passed to the LA through the open MV. In our previous fluid dynamics simulation study, we further showed that AVr resulted in excessive energy losses and high cardiac workload (Wong et al., 2023), which reduced the restoration of cardiac flow function. However, AVr promoted higher stroke volume and higher strains of myocardial tissues, and previous authors (Arzt et al., 2011; Wong et al., 2023) speculated that this higher deformational stimulus was beneficial to subsequent cardiac development. It was, however, noteworthy that our current study was limited to the acute outcomes of FAV. Later in gestation, AVr resolved or at least reduced in some of the post-FAV patients, which could lead to further normalization of function and biomechanics, as demonstrated in the virtual intervention scenarios, with no AVr. It is unclear how and why this happens, but given that this is a very positive event, further studies are warranted.

Our investigations of post-FAV scans provided validation that the stroke volume and myocardial strains indeed increased, while our FE simulations based on post-FAV scans confirmed that FAV indeed reduced AV valve

resistance and relieved the stenosis. However, our results suggested that stenosis was not fully relieved. This corroborated with our previous image-based fluid dynamics studies, where we estimated that although the AV effective orifice area doubled after FAV, it remained substantially lower than (about one-fifth that of) that of a healthy fetal heart (Wong et al., 2023). The increase in circumferential and longitudinal strains agreed with previous findings by Ishii et al. which showed FAV intervention to promote increased myocardial strains (Ishii et al., 2012).

Our studies of post-FAV scans and simulations also revealed that some fetal LV cases did not experience a great reduction in AV velocity or LV pressure, despite relief of the stenosis and LV fluid congestion. Clinically, we often used AV velocity and Bernoulli's equation to estimate valvular pressure gradient, and a failure to reduce AV velocity would have falsely implied that FAV did not relieve the stenosis. Our investigations, however, revealed that stenosis was indeed relieved for all cases, but there were likely other physiological responses, such as elevated myocardial contractile forces and peripheral vascular resistance, that negated the reduction of AV velocity and LV pressure. This complex interplay between various physiological features served as a reminder that we should not use simple single measures to assess stenosis severity during FAV, and a complete image-based FE model might be more appropriate. It seemed reasonable to expect some LVs to have elevated contractility after FAV intervention, which could be induced by the increased deformational stimuli of the LV and an end-diastolic distension of the LV due to AVr, in line with the Frank-Starling mechanism. In our results, myocardial contractility increased across FAV for all patients except Patient 1, whose myocardial contractility in fact maintained at a similar level despite a slight decrease (Figure 6G). Our sensitivity analysis showed that contractility changes had a significant effect on cardiac function and biomechanics. Contractility changes across FAV intervention was thus an important feature to consider. In terms of peripheral vascular resistance changes, our sensitivity analysis also suggested that this could occur after FAV intervention, and this seemed reasonable, as increased overall cardiac output brought by FAV intervention could have activated higher peripheral vascular tone. However, this physiological change had a milder effect.

Our modelling results demonstrated that patient-specific modeling can enable a detailed investigation of the complex biomechanical and physiological effects of FAV and was useful in capturing the individuality of each patient, addressing the large patient-to-patient variability. However, we found that the computational prediction of acute outcomes of FAV remained difficult, because it was not currently possible to predict how much of the stenosis

would be relieved by FAV intervention and how much (if any) the fetal heart contractility would alter, which is important as stenosis severity and contractility were shown to be very influential parameters with significant effects on simulation outcomes. However, it might be the case that with a much larger sample size, we can obtain the statistical distribution of these physiological changes after FAV, to help with computational predictions.

Finally, comparing features of patients that went on to be BV (Patient 1 and 2) or UV (Patient 3 and 4) post-FAV, our results showed that UV patients LVs remained relatively low pressure compared to the BV cases post-FAV, and they also had lower stroke volume, work done and myocardial contractility. This appeared to support the hypothesis that the biomechanically “weaker” fetal hearts were more likely to progress to a UV outcome, but the sample size here is low and cannot provide enough evidence to test this hypothesis. However, clinical estimations of LV pressure were made by Tulzer et al. and McElhinney et al., who concluded that the higher-pressure pre-FAV LVs have a greater chance of progressing to a BV outcome post-FAV (McElhinney et al., 2009; Tulzer et al., 2022). This corroborated the findings of our study.

There are several limitations of this study. Firstly, our biomechanics simulations required idealizations. For example, we assumed the same myocardial helix angle configuration for all LVs and applied the same myocardial stiffness across all cases. Further, our modelling of AVr and MVr were simplified, as a constant valve resistance across diastole and systole respectively, was assumed. Thirdly, fetal echo tended to have high levels of noise, which could have resulted in inaccuracies in our image-based computational modelling. This might account for some of the mismatch between virtual FAV and actual post-FAV measurements and simulations.

5.0 CONCLUSION

We conducted image-based computational modelling to understand the biomechanical impact of FAV interventom. Our virtual FAV simulations showed that FAV was likely to improve LV functionality, by depressurizing the LV and LA, reducing AV velocity and MVr velocity, reducing myofiber stress, and increasing stroke volume. The presence of AVr moderately inhibited LV depressurisation and could prevent LA depressurization, however, it provided substantial augmentation of stroke volume and myocardial strains, which could provide beneficial stimuli to further cardiac development. Through comparisons of virtual FAV intervention to actual post-FAV images and simulations, we found that cardiac contractility was likely to increase after FAV, which could cause unexpected

increases in AV forward velocities and LV pressure, contrary to the expectation that stenosis should decrease them. Post-FAV simulations demonstrated substantial stenosis relief, but AV resistance remained quite different from those of healthy hearts.

Supplementary Material

1.0 Demonstration of Cardiac Motion Estimation Pre- and Post-Fetal Aortic Valvuloplasty (FAV) Intervention

Demonstration of each patients cardiac motion tracking, pre- and post-FAV intervention, at end diastolic volume (EDV) and end systolic volume (ESV), Figure S1. Inner wall extracted to measure LV volume variation over the cardiac cycle.

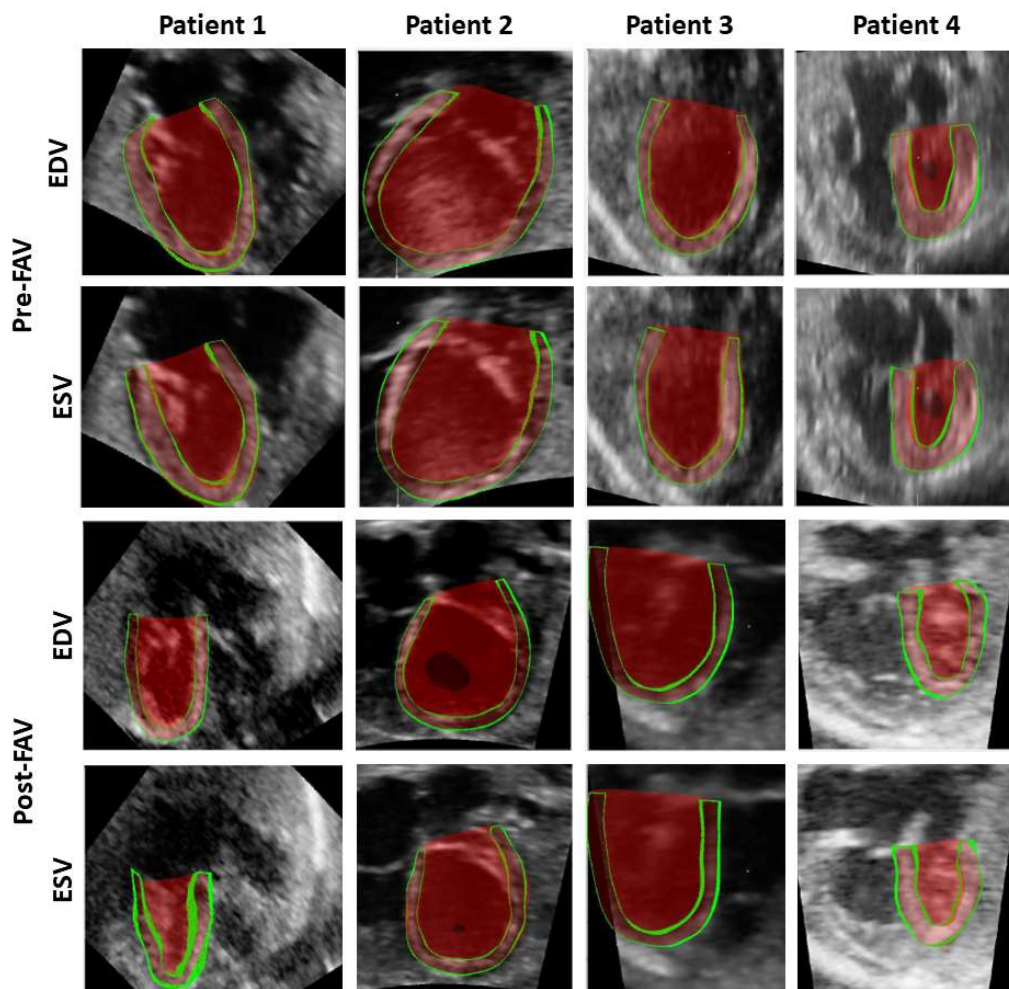


Figure S2. Reconstructed geometries superimposed onto associated echo image, green outline highlighting geometry proportion close to current image plane, for all patients pre- and post-FAV at EDV and ESV time points.

2.0 Retrospective Data Collection for Heart Rate Change Pre- to Post-FAV Intervention

Data retrospectively collected for aortic valve regurgitation (AVr) velocity, post FAV for $n=44$, and change in beats per minute (BPM), from pre- to post-FAV intervention for $n=34$ patients, Figure S2. Average AVr velocity post-FAV was 1.92 ± 0.87 m/s and the average BPM increased by 1.77% post-FAV compared to pre-FAV, with a standard deviation of ± 8.23 .

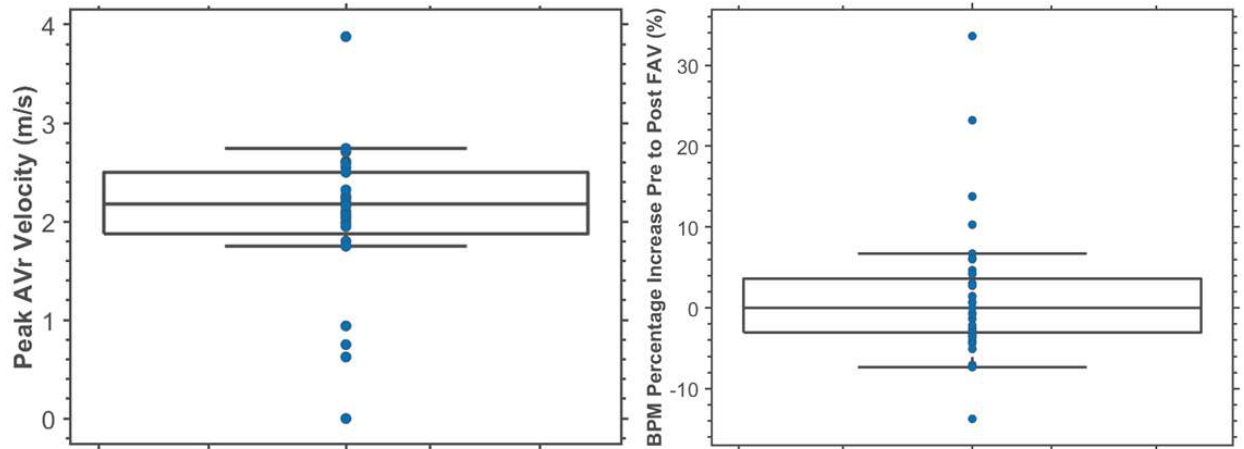


Figure S2. Bar plot showing AVr velocity post-FAV ($n=44$) and percentage increase in BPM, from pre- to post-FAV intervention ($n=34$).

3.0 Healthy Peak Systolic Myofiber Stress Data

Healthy peak systolic myofiber stress data extracted from the patient specific optimization methods ($n=6$). The optimisation protocol was the same as that described in main text section 2.5, for pre-FAV patient specific optimization, except for optimizing for valve resistances, as that was only required for the diseased modelling protocol. From Figure S3 there is a very weak negative correlation between peak

systolic myofiber stress and gestational age ($r=-0.10$), to compare the virtual intervention results the average peak systolic myofiber stress of 12.19 kPa was used.

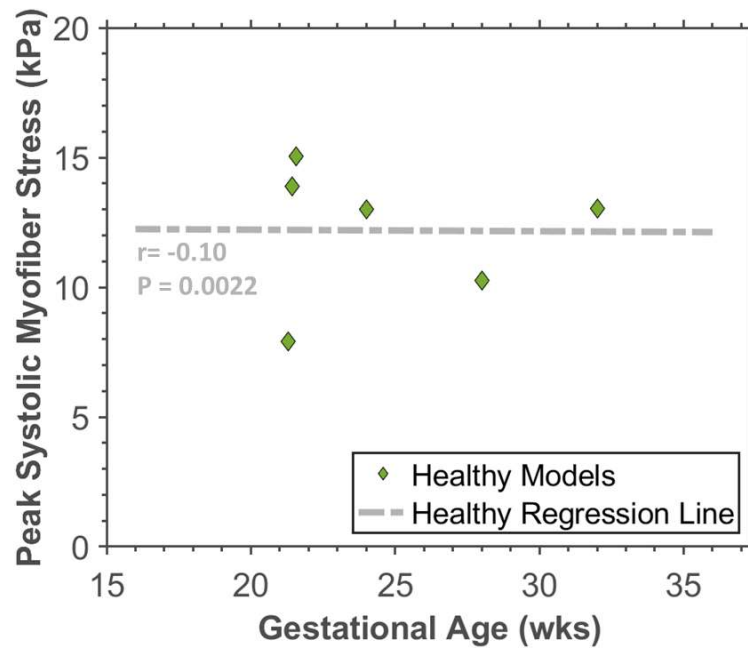


Figure S3. Relationship between peak systolic myofiber stress and gestational age, output from patient specific computational methods.

4.0 Pre- and Post-FAV Biomechanics Characteristics

Table S1 and S2 details the final match between image and simulated stroke volume, AV ΔP , MV ΔP , AVr ΔP and MVr ΔP , for all patients, for pre- and post-FAV patient-specific, image-based simulations, demonstrating a satisfactory match (Note: AVr ΔP not optimised for in pre-FAV models as not present). Errors for stroke volume were $-0.74 \pm 4.57\%$, while that for valve gradients were $-2.14 \pm 14.24\%$. Patient 3s post-FAV MVr ΔP was especially difficult to match, and had an error of 38%, which could be due cumulatively to errors in echo measurements and idealization assumptions of the FE and lumped parameter model.

Table S1. Image vs simulation match for all pre-FAV models.

	ID	Stroke Volume (ml)	AV ΔP (mmHg)	MV ΔP (mmHg)	MVr ΔP (mmHg)
Image	Patient 1	0.28	48.12	3.69	66.75
Simulation		0.31	47.60	3.32	65.39
Image	Patient 2	0.50	4.87	1.49	39.94
Simulation		0.50	5.65	2.02	36.32

Image	Patient 3	0.10	13.54	27.04	27.04
Simulation		0.10	13.91	27.30	27.30
Image	Patient 4	0.085	37.30	42.91	42.91
Simulation		0.084	39.59	42.56	42.56

Table S2. Image vs simulation match for all post-FAV models.

	ID	Stroke Volume (ml)	AV ΔP (mmHg)	MV ΔP (mmHg)	AVr ΔP (mmHg)	MVr ΔP (mmHg)
Image	Patient 1	0.45	22.66	3.62	19.36	48.96
Simulation		0.45	22.77	3.91	17.38	44.52
Image	Patient 2	0.71	8.02	2.54	25.00	53.40
Simulation		0.69	8.35	3.17	21.49	55.43
Image	Patient 3	0.25	2.86	1.69	13.99	38.44
Simulation		0.24	3.01	1.67	16.40	23.81
Image	Patient 4	0.31	13.96	2.15	20.43	32.21
Simulation		0.32	15.39	2.77	19.40	30.96

Pre- and post-FAV physiological characteristics from scans and biomechanics characteristics from simulations, as demonstrated in Figure 6, were also given here in Table S3. Age-matched LV pressure for a healthy heart was also given, based on intracardiac pressure measurements by (Johnson et al., 2000).

Table S3. Comparison of pre- and post-FAV fetal biomechanics, extracted from the patient specific computational methods.

	Patient 1 (BV outcome)		Patient 2 (BV outcome)		Patient 3 (UV outcome)		Patient 4 (UV outcome)	
	Pre-FAV	Post-FAV	Pre-FAV	Post-FAV	Pre-FAV	Post-FAV	Pre-FAV	Post-FAV
Stroke Volume (ml)	0.28	0.45	0.50	0.71	0.10	0.25	0.085	0.31
EDV (ml)	1.49	1.22	4.71	5.65	1.88	3.23	1.02	1.10
LV Pressure (mmHg)	73.55	50.69	49.72	63.15	35.83	40.34	50.14	34.96
Age-Matched Healthy Heart LV Pressure (Johnson et al.)	31.71	31.96	39.67	41.17	27.73	28.23	31.71	31.96
Work Done (mmHg ml)	21.05	16.35	15.93	32.46	2.22	5.16	2.98	8.74
Peak Myofiber Stress (kPa)	22.19	14.82	21.91	31.12	12.93	17.77	11.53	10.27
Myocardial Contractility (kPa)	39.59	37.41	27.64	48.31	16.78	20.73	21.65	23.77
Longitudinal Strain (%)	7.84	15.28	5.40	7.61	1.02	1.17	3.81	12.58
Circumferential Strain (%)	1.89	9.45	5.34	6.02	0.33	5.39	-0.52	8.22

REFERENCES

- Arzt, W., Wertaschnigg, D., Veit, I., Klement, F., Gitter, R., & Tulzer, G. (2011). Intrauterine aortic valvuloplasty in fetuses with critical aortic stenosis: Experience and results of 24 procedures. *Ultrasound in Obstetrics and Gynecology*, 37(6), 689–695. <https://doi.org/10.1002/uog.8927>
- Bradford, V. R., Tworetzky, W., Callahan, R., Wilkins-Haug, L. E., Benson, C. B., Porras, D., Guseh, S. H., Lu, M., Sleeper, L. A., Gellis, L., & Friedman, K. G. (2022). Hemodynamic and anatomic changes after fetal aortic valvuloplasty are associated with procedural success and postnatal biventricular circulation. *Prenatal Diagnosis*, July, 1312–1322. <https://doi.org/10.1002/pd.6216>
- Devore, G. R., Klas, B., Satou, G., & Sklansky, M. (2019). Evaluation of fetal left ventricular size and function using speckle-tracking and the simpson rule. *Journal of Ultrasound in Medicine*, 38(5), 1209–1221. <https://doi.org/10.1002/jum.14799>
- Finsberg, H., Xi, C., Tan, J. Le, Zhong, L., Genet, M., Sundnes, J., Lee, L. C., & Wall, S. T. (2018). Efficient estimation of personalized biventricular mechanical function employing gradient-based optimization. *International Journal for Numerical Methods in Biomedical Engineering*, 34(7), 1–20. <https://doi.org/10.1002/cnm.2982>
- Freud, L. R., McElhinney, D. B., Marshall, A. C., Marx, G. R., Friedman, K. G., del Nido, P. J., Emani, S. M., Lafranchi, T., Silva, V., Wilkins-Haug, L. E., Benson, C. B., Lock, J. E., & Tworetzky, W. (2014). Fetal aortic valvuloplasty for evolving hypoplastic left heart syndrome: postnatal outcomes of the first 100 patients. *Circulation*, 130(8), 638–645. <https://doi.org/10.1161/CIRCULATIONAHA.114.009032>
- Friedman, K. G., Schidlow, D., Freud, L., Escobar-Diaz, M., & Tworetzky, W. (2014). Left ventricular diastolic function and characteristics in fetal aortic stenosis. *American Journal of Cardiology*, 114(1), 122–127. <https://doi.org/10.1016/j.amjcard.2014.04.013>
- Friedman, K. G., Sleeper, L. A., Freud, L. R., Marshall, A. C., Godfrey, M. E., Drogosz, M., Lafranchi, T., Benson, C. B., Wilkins-Haug, L. E., & Tworetzky, W. (2018). Improved technical success, postnatal outcome and refined predictors of outcome for fetal aortic valvuloplasty. *Ultrasound in Obstetrics and Gynecology*, 52(2), 212–220. <https://doi.org/10.1002/uog.17530>
- Garcia-Canadilla, P., Dejea, H., Bonnin, A., Balicevic, V., Loncaric, S., Zhang, C., Butakoff, C., Aguado-Sierra, J., Vázquez, M., Jackson, L. H., Stuckey, D. J., Rau, C., Stampanoni, M., Bijnens, B., & Cook, A. C. (2018). Complex Congenital Heart Disease Associated With Disordered Myocardial Architecture in a Midtrimester Human Fetus. *Circulation. Cardiovascular Imaging*, 11(10), 1–10. <https://doi.org/10.1161/CIRCIMAGING.118.007753>
- Gardiner, H. M., Kovacevic, A., Tulzer, G., Sarkola, T., Herberg, U., Dangel, J., Öhman, A., Bartrons, J., Carvalho, J. S., Jicinska, H., Fesslova, V., Averiss, I., Mellander, M., Bullock, F., Shebani, S., Clur, S. A., Daehnert, I., Salvo, G. Di, Heying, R., ... Weil, J. (2016). Natural history of 107 cases of fetal aortic stenosis from a European multicenter retrospective study. *Ultrasound in Obstetrics and Gynecology*, 48(3), 373–381. <https://doi.org/10.1002/uog.15876>
- Green, L., Chan, W. X., Ren, M., Mattar, C., Chuan, L., Choon, L., & Yap, H. (2022). The dependency of fetal left ventricular biomechanics function on myocardium helix angle configuration. *Biomechanics and Modeling in Mechanobiology*, 22(1). <https://doi.org/10.1007/s10237-022-01669-z>
- Guccione, J. M., McCulloch, A. D., & Waldman, L. K. (1991). Passive material properties of intact ventricular myocardium determined from a cylindrical model. *Journal of Biomechanical Engineering*, 113, 42–55. <https://doi.org/10.1115/1.2795971>

- Guccione, J. M., Waldman, L. K., & McCulloch, A. D. (1993). Mechanics of active contraction in cardiac muscle: Part II—cylindrical models of the systolic left ventricle. *Journal of Biomechanical Engineering*, 115(1), 82–90. <https://doi.org/10.1115/1.2895474>
- Ishii, T., McElhinney, D. B., Harrild, D. M., Marcus, E. N., Sahn, D. J., Truong, U., & Tworetzky, W. (2012). Circumferential and longitudinal ventricular strain in the normal human fetus. *Journal of the American Society of Echocardiography*, 25(1), 105–111. <https://doi.org/10.1016/j.echo.2011.09.016>
- Ishii, T., McElhinney, D. B., Harrild, D. M., Marcus, E. N., Sahn, D. J., Truong, U., & Tworetzky, W. (2014). Ventricular strain in fetuses with aortic stenosis and evolving hypoplastic left heart syndrome before and after prenatal aortic valvuloplasty. *Fetal Diagnosis and Therapy*, 35(1), 18–26. <https://doi.org/10.1159/000341717>
- Johnson, P., Maxwell, D. J., Tynan, M. J., & Allan, L. D. (2000). Intracardiac pressures in the human fetus. *Heart*, 84(1), 59–63. <https://doi.org/10.1136/heart.84.1.59>
- Li, Y., Sun, J., Tang, C. K., & Shum, H. Y. (2004). Lazy snapping. *ACM Transactions on Graphics*, 303–308. <https://doi.org/10.1145/1186562.1015719>
- Mäkikallio, K., McElhinney, D. B., Levine, J. C., Marx, G. R., Colan, S. D., Marshall, A. C., Lock, J. E., Marcus, E. N., & Tworetzky, W. (2006). Fetal aortic valve stenosis and the evolution of hypoplastic left heart syndrome: Patient selection for fetal intervention. *Circulation*, 113(11), 1401–1405. <https://doi.org/10.1161/CIRCULATIONAHA.105.588194>
- Marshall, A. C., Tworetzky, W., Bergersen, L., McElhinney, D. B., Benson, C. B., Jennings, R. W., Wilkins-Haug, L. E., Marx, G. R., & Lock, J. E. (2005). Aortic valvuloplasty in the fetus: Technical characteristics of successful balloon dilation. *Journal of Pediatrics*, 147(4), 535–539. <https://doi.org/10.1016/j.jpeds.2005.04.055>
- McElhinney, D. B., Marshall, A. C., Wilkins-Haug, L. E., Brown, D. W., Benson, C. B., Silva, V., Marx, G. R., Mizrahi-Arnaud, A., Lock, J. E., & Tworetzky, W. (2009). Predictors of technical success and postnatal biventricular outcome after in utero aortic valvuloplasty for aortic stenosis with evolving hypoplastic left heart syndrome. *Circulation*, 120(15), 1482–1490. <https://doi.org/10.1161/CIRCULATIONAHA.109.848994>
- Mulieri, L. A., Hasenfuss, G., Leavitt, B., Allen, P. D., & Alpert, N. R. (1992). Altered myocardial force-frequency relation in human heart failure. *Circulation*, 85(5), 1743–1750. <https://doi.org/10.1161/01.CIR.85.5.1743>
- Nishitani, S., Torii, N., Imai, H., Haraguchi, R., Yamada, S., & Takakuwa, T. (2020). Development of helical myofiber tracts in the human fetal heart: Analysis of myocardial fiber formation in the left ventricle from the late human embryonic period using diffusion tensor magnetic resonance imaging. *Journal of the American Heart Association*, 9(19). <https://doi.org/10.1161/JAHA.120.016422>
- Ohayon, J., Usson, Y., Jouk, P. S., & Cai, H. (1999). Fibre orientation in human fetal heart and ventricular mechanics: A small perturbation. *Computer Methods in Biomechanics and Biomedical Engineering*, 2(2), 83–105. <https://doi.org/10.1080/10255849908907980>
- Ong, C. W., Ren, M., Wiputra, H., Mojumder, J., Chan, W. X., Tulzer, A., Tulzer, G., Buist, M. L., Mattar, C. N. Z., Lee, L. C., & Yap, C. H. (2020). Biomechanics of Human Fetal Hearts with Critical Aortic Stenosis. *Annals of Biomedical Engineering*. <https://doi.org/10.1007/s10439-020-02683-x>
- Parasuraman, R., Osmond, C., & Howe, D. T. (2013). Gestation-specific reference intervals for fetal cardiac Doppler indices from 12 to 40 weeks of gestation. *Open Journal of Obstetrics and Gynecology*, 03(01), 97–104. <https://doi.org/10.4236/ojog.2013.31019>

- Pennati, G., Bellotti, M., & Fumero, R. (1997). Mathematical modelling of the human foetal cardiovascular system based on Doppler ultrasound data. *Medical Engineering and Physics*, 19(4), 327–335. [https://doi.org/10.1016/S1350-4533\(97\)84634-6](https://doi.org/10.1016/S1350-4533(97)84634-6)
- Pennati, G., & Fumero, R. (2000). Scaling approach to study the changes through the gestation of human fetal cardiac and circulatory behaviors. *Annals of Biomedical Engineering*, 28(4), 442–452.
- Pickard, S. S., Wong, J. B., Bucholz, E. M., Newburger, J. W., Tworetzky, W., Lafranchi, T., Benson, C. B., Wilkins-Haug, L. E., Porras, D., Callahan, R., & Friedman, K. G. (2020). Fetal Aortic Valvuloplasty for Evolving Hypoplastic Left Heart Syndrome: A Decision Analysis. *Circulation: Cardiovascular Quality and Outcomes*, 13(April), 32–41. <https://doi.org/10.1161/CIRCOUTCOMES.119.006127>
- Racca, A. W., Klaiman, J. M., Pioner, J. M., Cheng, Y., Beck, A. E., Moussavi-Harami, F., Bamshad, M. J., & Regnier, M. (2016). Contractile properties of developing human fetal cardiac muscle. *Journal of Physiology*, 594(2), 437–452. <https://doi.org/10.1113/JP271290>
- Ren, M., Chan, W. X., Green, L., Armstrong, A. K., Tulzer, A., Tulzer, G., Buist, M. L., & Yap, C. H. (2023). Contribution of Ventricular Motion and Sampling Location to Discrepancies in 2D versus 3D Fetal Ventricular Strain Measures. *Journal of the American Society of Echocardiography*. <https://doi.org/10.1016/j.echo.2022.12.024>
- Shavik, S. M., Jiang, Z., Baek, S., & Lee, L. C. (2018). High spatial resolution multi-organ finite element modeling of ventricular-arterial coupling. *Frontiers in Physiology*, 9(119). <https://doi.org/10.3389/fphys.2018.00119>
- Tulzer, A., Arzt, W., Gitter, R., Sames-Dolzer, E., Kreuzer, M., Mair, R., & Tulzer, G. (2022). Valvuloplasty in 103 fetuses with critical aortic stenosis: outcome and new predictors for postnatal circulation. *Ultrasound in Obstetrics and Gynecology*, 59(5), 633–641. <https://doi.org/10.1002/uog.24792>
- Versmold, H. T., Kitterman, J. A., Phibbs, R. H., Gregory, G. A., & Tooley, W. H. (1981). Aortic blood pressure during the first 12 hours of life in infants with birth weight 610 to 4,220 grams. *Pediatrics*, 67(5), 607–613.
- Wiputra, H., Chan, W. X., Foo, Y. Y., Ho, S., & Yap, C. H. (2020). Cardiac motion estimation from medical images: a regularisation framework applied on pairwise image registration displacement fields. *Scientific Reports*, 10(1). <https://doi.org/10.1038/s41598-020-75525-4>
- Wohlmuth, C., Wertaschnigg, D., Wieser, I., Arzt, W., & Tulzer, G. (2016). Tissue Doppler imaging in fetuses with aortic stenosis and evolving hypoplastic left heart syndrome before and after fetal aortic valvuloplasty. *Ultrasound in Obstetrics and Gynecology*, 47(5), 608–615. <https://doi.org/10.1002/uog.14885>
- Wong, H. S., Li, B., Tulzer, A., Tulzer, G., & Yap, C. H. (2023). Fluid Mechanical Effects of Fetal Aortic Valvuloplasty for Cases of Critical Aortic Stenosis with Evolving Hypoplastic Left Heart Syndrome. *Annals of Biomedical Engineering*. <https://doi.org/10.1007/s10439-023-03152-x>
- Wong, H. S., Wiputra, H., Tulzer, A., Tulzer, G., & Yap, C. H. (2022). Fluid Mechanics of Fetal Left Ventricle During Aortic Stenosis with Evolving Hypoplastic Left Heart Syndrome. *Annals of Biomedical Engineering*. <https://doi.org/10.1007/s10439-022-02990-5>
- Zheng, Y., Chan, W. X., Charles, C. J., Richards, A. M., Lee, L. C., Leo, H. L., & Yap, C. H. (2022). Morphological, functional, and biomechanical progression of LV remodelling in a porcine model of HFpEF. *Journal of Biomechanics*, 144(October), 111348. <https://doi.org/10.1016/j.jbiomech.2022.111348>
- Zheng, Y., Chan, W. X., Nielles-Vallespin, S., Scott, A. D., Ferreira, P. F., Leo, H. L., & Yap, C. H. (2023). Effects of myocardial sheetlet sliding on left ventricular function. *Biomechanics and Modeling in Mechanobiology*, 22(4), 1313–1332. <https://doi.org/10.1007/s10237-023-01721-6>

